Impact of ocean vertical mixing parameterization on Arctic sea ice and upper ocean properties using the NEMO-SI3 model

Sofia Allende[1], Anne Marie Treguier[2], Camille Lique[2], Clément de Boyer Montégut[2], François Massonnet[1], Thierry Fichefet[1], and Antoine Barthélemy[1]

[1]Earth and Climate Research, Earth and Life Institute, Université catholique de Louvain, Louvain-la-Neuve, Belgium
[2]Univ Brest, CNRS, IRD, Ifremer, Laboratoire d'océanographie physique et spatiale, IUEM, 29280, Plouzané, France
Correspondence: sofia.allende@uclouvain.be

Abstract.

We evaluate the vertical turbulent kinetic energy (TKE) mixing scheme of the NEMO-SI3 ocean–sea ice model in sea ice-covered regions of the Arctic Ocean. Specifically, we assess the parameters involved in the TKE mixed layer penetration (MLP) parameterization. This ad-hoc parameterization aims to capture processes like near-inertial oscillations, ocean swells, and waves that impact the ocean surface boundary layer, often not well-represented in the default TKE scheme. We evaluate this parameterization for the first time in three regions of the Arctic Ocean: the Makarov, Eurasian, and Canada Basins.

We demonstrate the strong effect of the scaling parameter that accounts for the presence of sea ice. Our results confirm that the TKE MLP must be scaled down below sea ice to avoid unrealistic deep mixed layers. The other parameters evaluated are the percentage of energy penetrating below the mixed layer and the length scale of its decay with depth. All these parameters affect the mixed layer depth and its seasonal cycle, the surface temperature and salinity, as well as the underlying stratification. Shallow mixed layers are associated with stronger stratification and fresh surface anomalies, and deeper mixed layers correspond to weaker stratification and salty surface anomalies.

Notably, we observe significant impacts on sea ice thickness across the Arctic Ocean in two scenarios: when the scaling parameter due to sea ice is absent and when the TKE mixed layer penetration process vanishes. In the former case, we observe an increase of several meters in the mixed layer depth together with a reduction in sea ice thickness ranging from 30 to 40 centimeters, reflecting the impact of stronger mixing. Conversely, in the latter case, we notice that a smaller mixed layer depth is accompanied by a moderate increase in sea ice thickness, ranging from 10 to 20 centimeters, as expected from a weaker mixing. Additionally, inter-annual variability suggests that experiments incorporating a scaling parameter based on sea ice concentration display an increased mixed layer depth during periods of reduced sea ice, which is consistent with observed trends. These findings underscore the influence, through specific parameterizations, of enhanced ocean mixing on the physical properties of the upper ocean and sea ice.

1 Introduction

In the last decades, global climate change has strongly affected the Arctic region, leading to a fast decrease in sea ice extent (Perovich and Richter-Menge, 2009). This phenomenon, together with the increase of openings in the ice pack, modifies the exchanges between the atmosphere and ocean and hence the fully-coupled atmosphere–sea ice–ocean system in the Arctic (McPhee, 2008). These changes have, in turn, led to alterations in the physical properties of the upper ocean, with implications for sea ice dynamics and response (Lenn et al., 2022). The upper layer of the Arctic Ocean, known as the Arctic mixed layer (ML), plays a pivotal role in regulating interactions between the deeper ocean, sea ice, and the atmosphere. Key factors influencing the Arctic ML include heat, freshwater and momentum fluxes generated by ocean-atmosphere exchanges, currents, tides and waves (Rabe et al., 2022; Rudels and Carmack, 2022). Observational data from the past few decades reveal changes in both winter and summer ML across the high Arctic, accompanied by changes in ocean stratification (Cole and Stadler, 2019; Peralta-Ferriz and Woodgate, 2015). These rapid transformations of the Arctic environment have far-reaching implications for climate and socio-economic aspects (Ford et al., 2021). Therefore, achieving an accurate representation of the Arctic Ocean and sea ice in models is essential to understanding and predicting these consequential changes.

Sea ice-ocean general circulation models used in coupled models assessed by the IPCC (Cassotta et al., 2022) exhibit significant discrepancies in the Arctic ML depth (Allende et al., 2023), which is directly influenced by vertical mass and momentum exchanges between the upper ocean and sea ice. These small scale vertical processes are parameterized in general circulation models. The NEMO-SI3 ocean-sea ice model (Madec et al., 2017; Sea-Ice-Working-Group et al., 2020) includes a vertical turbulent kinetic energy (TKE) closure scheme initially proposed by Blanke and Delecluse (1993). The scheme is complemented with an additional source of TKE to simulate the effects of near-inertial oscillations, ocean swells, and waves, specifically known as TKE mixed layer penetration. The TKE mixed layer penetration has been introduced to overcome summer biases in the mixed layer, which was too shallow in the Southern Ocean (Calvert and Siddorn, 2013; Rodgers et al., 2014). It redistributes a percentage of the surface TKE below the mixed layer depth. Moreover, the TKE mixed layer penetration is attenuated in the presence of sea ice. Previous research, such as that by Calvert and Siddorn (2013), has emphasized the impact of this parameterization on ocean properties in regions without sea ice. Additionally, Heuzé et al. (2015) has underscored the effect of this parameterization on deep convection in the Southern Ocean. However, the specific influence of TKE mixed layer penetration under sea ice has not been documented in the literature, although preliminary research carried out within the ArcticMix project (https://marine.copernicus.eu/about/research-development-projects/2016-2018/arcticmix) suggests that this influence is large. This is an important issue, because the NEMO-SI3 ocean–sea ice model is extensively used in polar climate studies (e.g. Goosse et al., 2023; Dong et al., 2023; Docquier et al., 2017; Vancoppenolle et al., 2008) and featured in the IPCC Assessment Reports.

This study aims to evaluate the impact of changes in the TKE mixed layer penetration in three distinct ice-covered regions within the Arctic Ocean: the Makarov, Eurasian, and Canada Basins. The Makarov Basin, located north of Siberia, experiences seasonal ice cover and receives freshwater from the East Siberian Sea. Shallow depths (500-1500 m) render it highly sensitive to sea ice variability and freshwater inputs. The Eurasian Basin extends from the Siberian Shelf to the North Pole, featuring

extensive multi-year ice cover and significant freshwater discharge from major Arctic rivers. Depths can reach 4000 m, influencing Arctic freshwater storage and sea ice dynamics. The Canada Basin, situated between North America and Siberia, is dominated by multi-year ice influenced by the Beaufort Gyre. Its complex bathymetry, including deep ridges like Alpha and Mendeleev, affects ocean circulation patterns and carbon cycling. Sea ice and upper ocean physical properties are closely linked due to mass and momentum exchanges at the ice-ocean boundary, exhibiting seasonal variations. In fall and winter, seawater freezes, and sea ice forms, accompanied by brine rejection. This process involves the rejection of salt from the crystal structure of water ice, increasing salinity in the upper ocean layer. Consequently, ocean stratification weakens, leading to a deeper ML. In spring and summer, as sea ice melts, freshwater is released into the ocean, reducing salt concentration and strengthening ocean stratification, thereby causing the ML to become shallower. By varying the parameters within this scheme, we illustrate how ocean and sea ice physical properties respond to alterations in upper ocean mixing. The paper is organized as follows. Section 2 gives a description of the NEMO-SI3 configuration, parameters, and outputs involved in the study, as well as the oceanic and sea ice observation data. Section 3 presents a diagnosis of the seasonal and inter-annual variability of the upper ocean and sea ice properties in 3 regions of the Arctic Ocean, by varying the mixing scheme. Finally, Section 4 presents concluding remarks and discusses the implications of our work.

2   Method

The vertical turbulent kinetic energy (TKE) closure scheme implemented in NEMO is based on the model developed by Bougeault and Lacarrere (1989) for the atmospheric boundary layer. It was subsequently adapted for an oceanic context by Gaspar et al. (1990) and integrated by Blanke and Delecluse (1993) into the OPA model, which is the ocean model component of the NEMO platform. In essence, this TKE turbulent closure model provides a prognostic for the evolution of turbulent kinetic energy ($\bar{e}$) and a closure assumption for turbulent length scales, both necessary for computing vertical eddy viscosity and diffusivity coefficients. The prognostic equation is given by:

$$\frac{\partial \bar{e}}{\partial t} = K_m \left(\frac{\partial \bar{U}_h}{\partial z} \right)^2 - K_\rho N^2 + \frac{\partial}{\partial z} \left(K_e \frac{\partial \bar{e}}{\partial z} \right) - \varepsilon. \tag{1}$$

It results from the balance between the vertical shear, the dissipation of TKE due to buoyancy, the vertical diffusion of TKE, and the energy dissipation. The last version of NEMO includes significant modifications introduced by Madec et al. (2017). These changes include considerations such as turbulent length scale adjustments that impose an extra assumption regarding the vertical gradient of the computed length scale (Madec et al., 1997). Additionally, a surface wave breaking parameterization has been incorporated following Mellor and Blumberg (2004), addressing the impact of surface wave breaking energetics. The model now accounts for Langmuir cells using a simple parameterization proposed by Axell (2002) for a $k - \epsilon$ turbulent closure. Furthermore, the TKE turbulent closure has been updated to include mixing just below the mixed layer. Our study focuses on evaluating the influence of this last modification, which we will refer to as TKE Mixed Layer Penetration (MLP). This parameterization has been introduced to address the underestimation of the ML depth (MLD), especially in situations characterized by windy conditions during summer months, as observed in the Southern Ocean (Rodgers et al., 2014). This

parameterization aims to account for observed phenomena that impact the density structure of the ocean's surface boundary layer. These include near-inertial oscillations, ocean swells, and waves, which are not fully captured by the default TKE scheme.

The TKE $\bar{e}(t,z)$ includes an additional energy source term $\bar{e}_{inertial}(t,z)$, which represents the contribution of the TKE MLP as:

$$\bar{e}_{inertial}(t,z) = \begin{cases} \chi \, f_r \, \bar{e}_{surf} \, \exp^{-z/h_\tau}, & \text{if } z > 0. \\ 0, & \text{if } z = 0. \end{cases} \tag{2}$$

Here, z is the depth, f_r, is the fraction of the surface TKE $\bar{e}_{surf}$ that penetrates into the ocean, and it takes values from 0 to 0.1. h_τ is the vertical mixing length scale that controls the exponential shape of the penetration. It can be set as either a uniform 10 m value, as a latitude-dependent value, which varies from 0.5 m at the equator to 30 m north to $40°$ latitude, or with a different value in the two hemispheres, see Fig. 2 of Storkey et al. (2018). The penetration scales of 10 and 30 m are illustrated in the left panel of Fig.1; 10 m was found optimal in the north Pacific (Calvert and Siddorn, 2013), while 30 m was required to improve the ML in the Southern Ocean (Storkey et al., 2018). The degree of this mixing is regulated by the scaling parameter χ in response to the presence of sea ice. When $\chi = 1$, there is no influence from ice cover; $\chi = 1 - \tanh(10\,f_i)$ where f_i represents the sea ice concentration fraction, $\chi = 1 - f_i$, and $\chi = 1 - \min(1, 4\,f_i)$ used to suppress TKE input into the ocean when sea ice concentration exceeds 25% (see right panel of Fig. 1).

To carry out this investigation, we utilize the NEMO4.2 version with the SI3 sea ice model, using the eORCA1 configuration. The eORCA1 quasi-isotropic global tripolar grid has a nominal resolution of $1°$, extended to the south to better represent the contribution of Antarctic under-ice shelf seas to the Southern Ocean freshwater cycle. The grid has a latitudinal grid refinement of $1/3°$ in the equatorial region. The vertical discretization consists of 75 levels, where the initial layer thicknesses increase non-uniformly from 1 m at the surface to 10 m at 100 m depth, reaching 200 m at the bottom. The atmospheric forcing for the ocean is provided by the ERA-5 reanalysis (Hersbach et al., 2020). In our simulations, we configure the setup to exclude salinity restoring under sea ice. This means that no flux correction on freshwater fluxes was applied. The default parameters are configured in NEMO4.2 as follows: $f_r = 0.08$, $\chi = 1 - \min(1, 4\,f_i)$ and $h_\tau = 30$ m, constituting the control run for our analysis. This specific configuration slightly differs from the NEMO4.2 reference one by increasing f_r from 0.05 to 0.08 to achieve a more realistic MLD in the Southern Ocean. The global ORCA1 configuration has been used in CMIP6 by 6 different groups who made different choices for the TKE MLP parameterization (table 1). CCCma, CMCC and CNRM used the default NEMO settings (note that although χ had not yet been introduced in NEMO3.4, the $(1 - f_i)$ factor was present by default). As noted above, the MOHC group introduced an additional option for h_τ (Storkey et al., 2018). EC-Earth and IPSL opted to turn off the MLP parameterization, because doing so improved the Atlantic Meridional Overturning Circulation (AMOC) in their coupled models. These different choices underline the need for further investigation of the MLP parameterization.

We have performed a series of sensitivity experiments to assess the impact of the TKE MLP on sea ice in the Arctic region. Our strategy is to perform long experiments (from January 1960 to December 2022) to assess possible long-term climate impacts. For this reason, the number of simulations is limited, and parameters are modified one at a time. We systematically
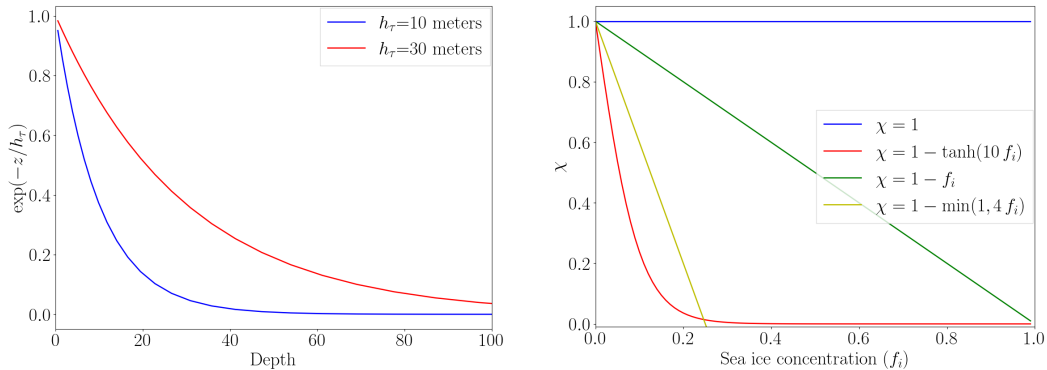
Figure 1. Left panel: Exponential penetration as a function of depth, for the two values of the vertical mixing length scale h_τ. Right panel: scaling parameter χ as a function of the sea ice concentration fraction f_i, for the four options of the scaling parameter χ.

Table 1. Configuration details of the TKE MLP parameterization in NEMO ocean models from various climate modeling groups participating in CMIP6-OMIP. The table provides information about the modeling group, NEMO version, and the values of f_r, χ, and h_τ north to $40°$.

Group	Model	Version	f_r	h_τ	χ
CCCma	CanESM5.0	NEMO3.4	0.05	30 m	$1 - f_i$
CMCC	CMCC-CM2-SR5	NEMO3.6	0.05	30 m	$1 - f_i$
CNRM	CNRM-CM6-1	NEMO3.6	0.05	30 m	$1 - f_i$
Ec-Earth	Ec-Earth	NEMO3.6	-	-	-
IPSL	IPSL-CM6A-LR	NEMO3.6	-	-	-
MOHC	HadGEM3-GC3.1-LL	NEMO3.6	0.05	10 m	$1 - f_i$

modify the parameters as outlined below: f_r ranges uniformly from 0 to 0.1, with values of 0, 0.005, 0.025, 0.075, and 0.1. Please note that using $f_r = 0$ leads to the same results as turning off the MLP parameterization, which means $\bar{e}_{inertial}(t, z) = 0$. In addition, we investigate the two values for h_τ (10 and 30 m) and the four options for χ: $\chi = 1$, $\chi = 1 - \tanh(10 f_i)$, $\chi = 1 - f_i$ and $\chi = 1 - \min(1, 4 f_i)$.

125   To investigate the variations in ocean and sea ice properties, we rely on monthly average outputs. Our analysis focuses on the following variables:

– Ocean variables: ocean mixed layer depth, for which the model follow the common threshold density criteria $\Delta\rho = \rho(z) - \rho(z_{ref}) = 0.03 \ kg/m^3$, with $z_{ref} = 0.5$ m; seawater potential density vertical profile in kg/m^3, sea water potential temperature vertical profile in $°C$, and the seawater salinity vertical profile in pss;

130   – Sea-ice variables: sea ice concentration, defined as the percentage of the grid cell covered by sea ice, and sea ice thickness, defined as the total volume of sea ice divided by grid-cell area in m.

We evaluate the performance of the NEMO-SI3 model using different sets of observational data and a reanalysis. Specifically, we employ the MLD climatology from IFREMER-LOPS, developed by de Boyer Montégut C. (2024). In the following, we refer to this data set as the LOPS climatology. This dataset provides monthly MLD, sea surface temperature and sea surface
135 salinity values across the global ocean at a spatial resolution of $1°$ by $1°$. The climatology is constructed based on approximately 7.3 million temperature and salinity profiles collected at sea between January 1970 and December 2021. This includes data from the ARGO program, the NCEI-NOAA World Ocean Database (Boyer et al., 2018), and Ice-Tethered Profilers (ITP). The MLD is calculated for each individual profile by employing the threshold density criterion. This criterion is based on the difference in density between a given depth (z) and a reference depth ($= z_{ref}$), which is denoted as $\Delta\rho = \rho(z) - \rho(z_{ref})$. The MLD is
140 then defined as the depth where this difference in density exceeds the threshold value of 0.03 kg/m^3 (e.g. de Boyer Montégut et al. (2004)). The LOPS climatology estimates the MLD as the depth mixed over at least one daily cycle, typically assumed to be no less than 10 m deep (e.g., Brainerd and Gregg (1995)). This depth filters out possible daily stratification in the top few meters, which is common in the tropics or summer mid-latitudes. However, in the Arctic Ocean, where the diurnal cycle linked to solar heat fluxes is minimal or nonexistent, especially with ice present, the MLD can be shallower than the usual 10 m
145 depth (e.g., Peralta-Ferriz and Woodgate (2015)). Therefore, we have recomputed the MLD for the Arctic region using a more appropriate reference depth of 5 meters. Additionally, to study the inter-annual variability of the MLD, we directly computed the MLD from individual ITP data (Toole et al., 2011; Krishfield et al., 2008) using completed missions available at the WHOI website. We computed vertical potential density profiles using the TEOS-10 Gibbs Sea Water toolbox (McDougall and Barker, 2011), and determined the MLD by applying the threshold density criteria. This was done to compare ITP observational data
150 with NEMO sensitivity experiments, where the surface reference depth for ITP varies from 10 to 0 m depending on the profile. The ITP data are from 2004 until 2019, with the majority of the observations between the years 2007 to 2015. Our study also incorporates temperature and salinity vertical profiles provided by the latest version of the World Ocean Atlas 2023 (WOA23), which integrates data from 1955 to 2022 at a resolution of $1°$ (Reagan et al., 2023).

The sea ice concentration observational data used in this study is the EUMETSAT OSI-SAF (Lavergne et al., 2019). This
155 dataset is available at the Copernicus Climate Change Service Climate Data Store, and it provides coarse-resolution information based on measurements from various sensors, including the Scanning Multichannel Microwave Radiometer from 1979 to 1987, the Special Sensor Microwave/Imager from 1987 to 2006, and the Special Sensor Microwave Imager/Sounder from 2005 onward. The dataset covers the period from 1979 to the present day and is regularly updated. The grid resolution of this dataset is 25 km. In addition, we employ the Pan-Arctic Ice-Ocean Modeling and Assimilation System (PIOMAS), a coupled
160 model that integrates ocean and sea ice and assimilates daily satellite-derived products for sea ice concentration and sea surface temperature (Zhang and Rothrock, 2003). The PIOMAS dataset covers the period from 1978 to the present, including Arctic sea ice thickness, which is utilized in this study.
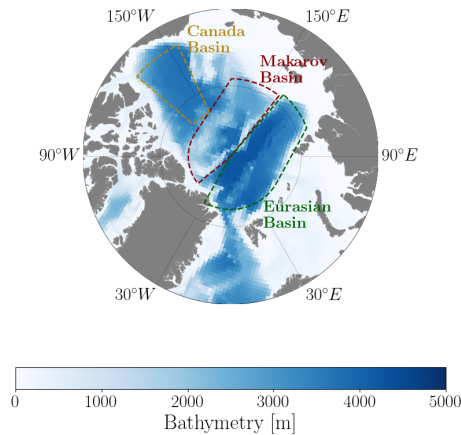
Figure 2. Bathymetry in meters of the ORCA1 configuration, derived from the ETOPO2 dataset. Dashed color lines show the boundaries of the Makarov (in red), Eurasian (in green) and Canada (in yellow) Basins following Peralta-Ferriz and Woodgate (2015).
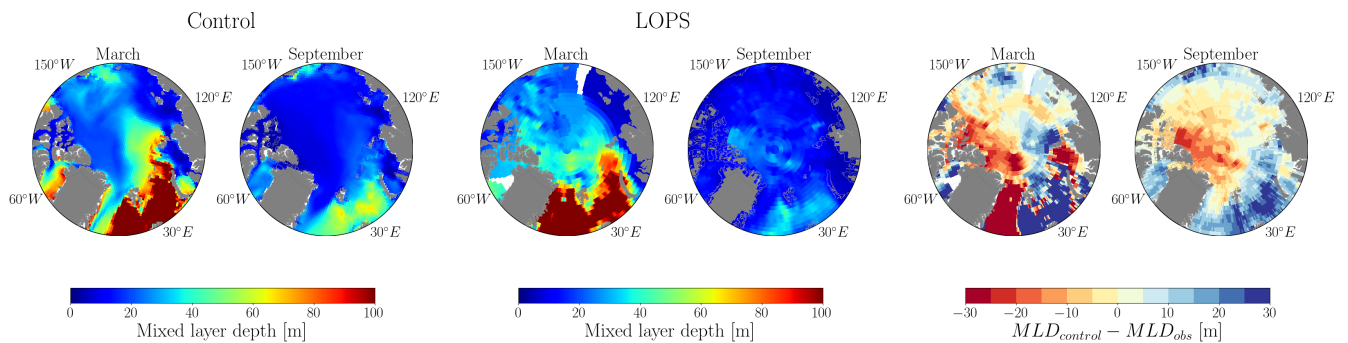
Figure 3. MLD maps of the control simulation, the LOPS climatology, and the differences between both in March and September. Data is averaged in time between 1970-2021.

3 Results

Our analysis focuses on the Arctic region, specifically the Makarov, Eurasian, and Canada Basins, which are characterized by year-round sea ice coverage. These regions are defined as follows: The Makarov Basin (83.5–90°N between 50–180°W and 78–90°N between 141–180°E), the Eurasian Basin (82–90°N between 30°W–140°E and 78–82°N between 110–140°E), and the Canada Basin (72–84°N and 130–155°W)–see Fig. 2.

3.1 Upper ocean properties

Fig. 3 illustrates the spatial distribution of mixed layer depth from control run and LOPS climatology in both March and September. Model outputs have been averaged from January 1970 to December 2021, corresponding to the same years as the MLD from LOPS climatology. We observe that the MLD is generally underestimated by the model in September and
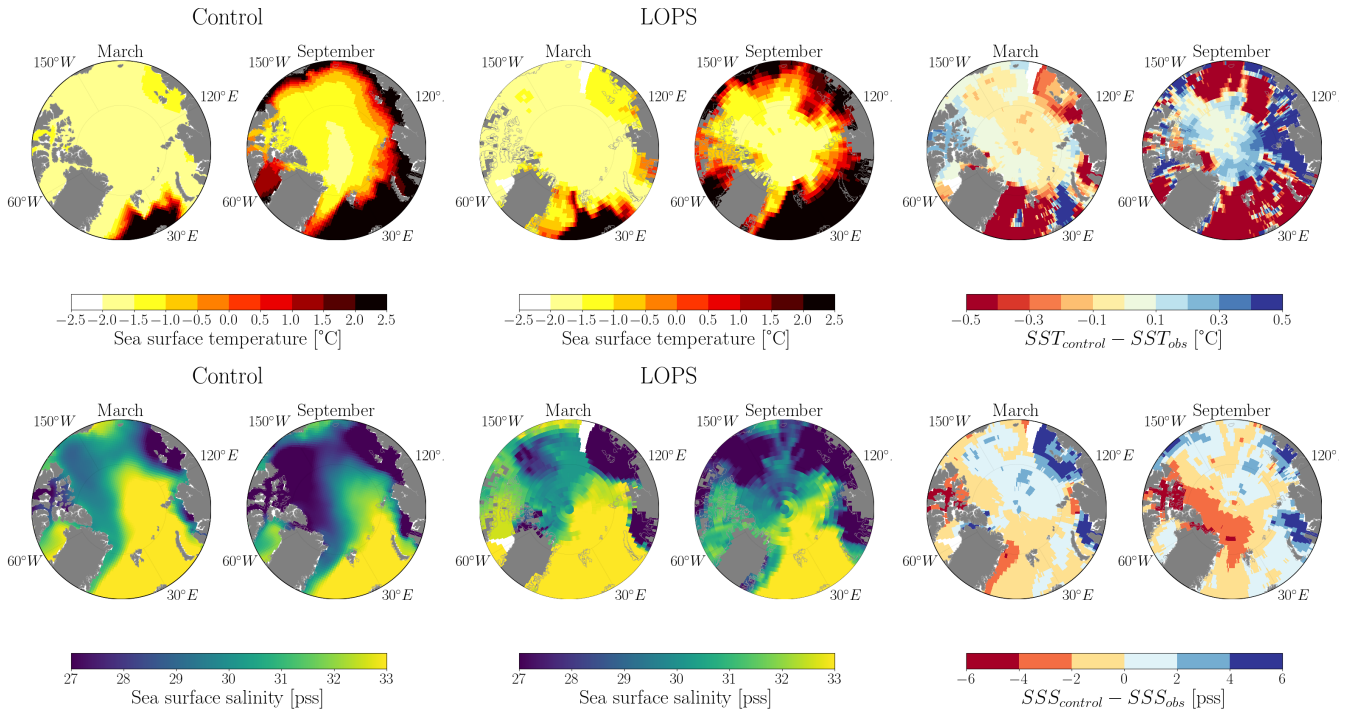
Figure 4. Sea surface temperature and sea surface salinity maps of the control simulation, the LOPS climatology and the differences between both in March and September in the pan-Arctic region. Data is averaged in time between 1970-2021.

March in the Arctic Basins, especially for the area of the Makarov and Eurasian Basins next to Greenland, where the model underestimates the MLD by tens of meters. Compared to a large portion of global models forced by CORE-II and JRA55-do, as studied by Ilıcak et al. (2016) and Allende et al. (2023), which include both NEMO and non-NEMO models, MLD discrepancies with observational data are less pronounced. The area along the east coast of Greenland presents pronounced MLD differences in March, with shallower ML in the model than in the LOPS climatology. That region is covered with ice at that time of the year and no MLD observations exist there, while deeper ML are measured further offshore in the open and deep ocean. The climatology might result in an overestimation of MLD along that coast, relying on the only data present offshore for its mapping. This would be one point to be improved in a future version of this climatology. Furthermore, Fig. 4 displays the spatial distribution of sea surface temperature and salinity for the control run and LOPS climatology. The sea surface temperature from the control run aligns with LOPS values for March and September in the three regions studied here. However, the March sea surface salinity from the control run appears to be saltier compared to the LOPS climatology over the Canada Basin and the eastern region of the Eurasian Basin, while it appears fresher than LOPS climatology in the region next to Greenland and the western part of the Makarov Basin in September.

We now investigate the sensitivity of the seasonal cycle of the MLD to the TKE MLP parameters previously introduced in Section 2. We individually modify each parameter from the control run, with each simulation named to indicate the new value
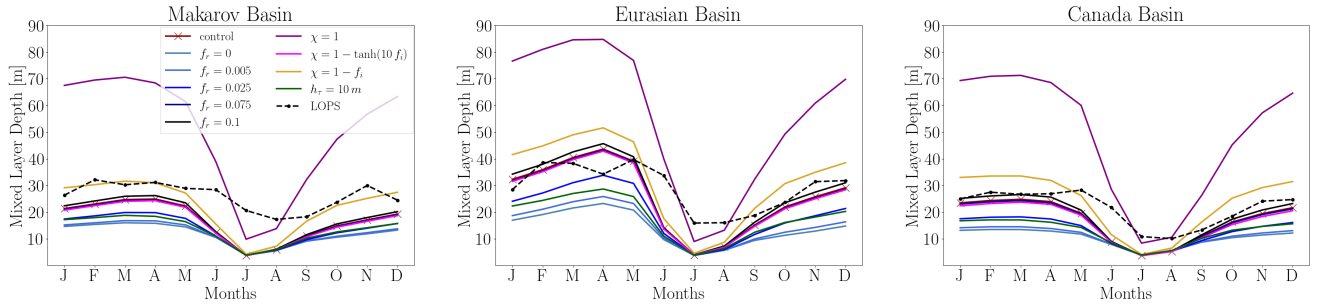
Figure 5. Seasonal cycle of the MLD in the Makarov, Eurasian and Canada Basins. Data is averaged in time between 1970-2021.
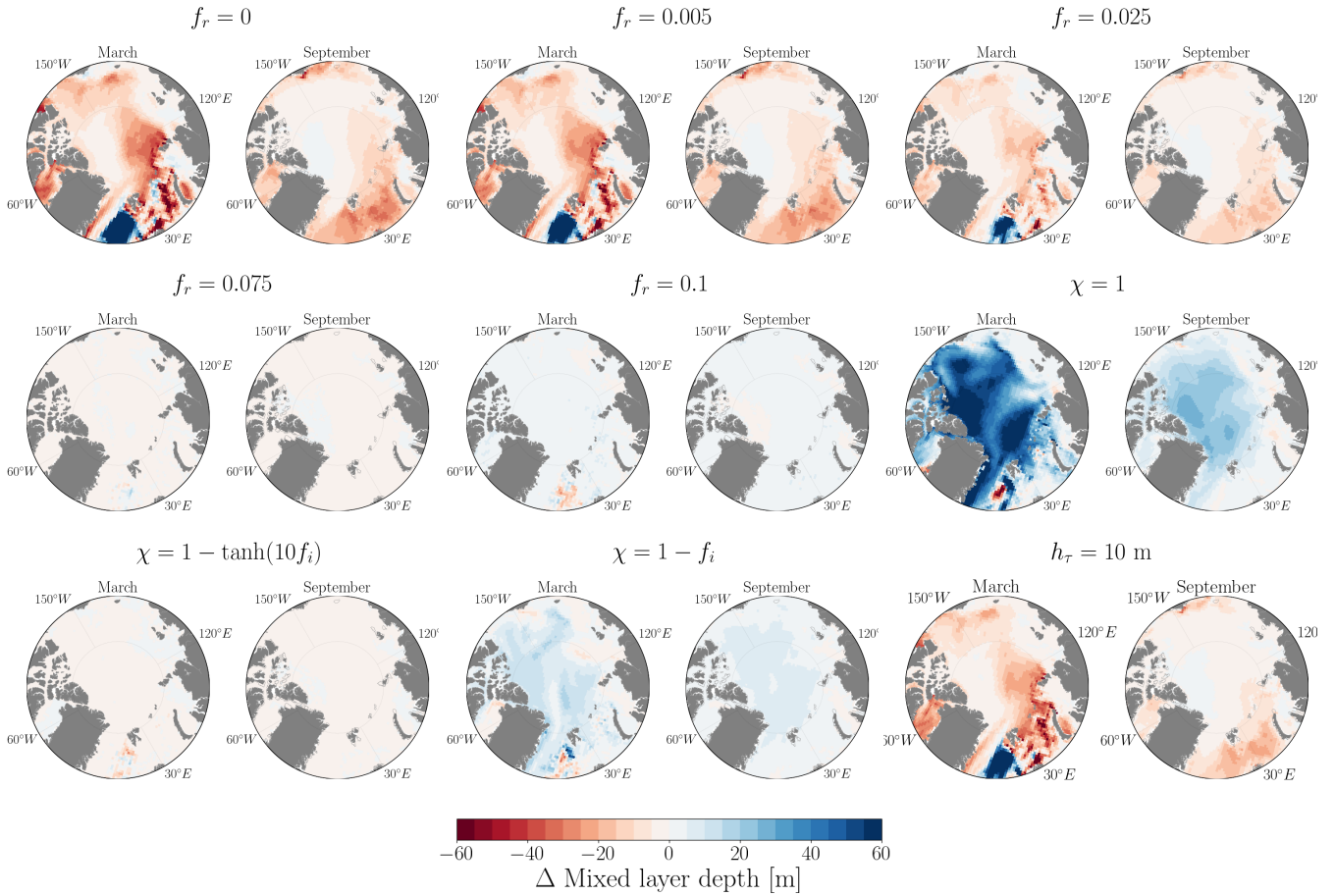
Figure 6. Maps displaying the differences in MLD between the sensitivity experiment (the title indicates the parameter modified) and the control run in March and September. Data is averaged in time between 1970-2021.

of the parameter relative to the control simulation. Figure 5 illustrates the MLD seasonal cycle from the sensitivity experiments, the control run, and the LOPS climatology in each region. Data is averaged spatially and temporally for each basin. We observe similar behavior in all three regions when the TKE MLP parameters are varying. The most considerable difference between models is observed in the simulation with no attenuation to account for sea ice coverage ($\chi = 1$). In such a case, a significant TKE MLP mixing is induced, resulting in a deeper ML for all months compared to other simulations. When using the other three options for the scaling parameter of the TKE MLP (i.e., $\chi = 1 - \tanh(10 f_i)$, $\chi = 1 - f_i$ and $\chi = 1 - \min(1, 4 f_i)$), the MLD values are closer to the LOPS climatology. We observe that both the control run ($\chi = 1 - \min(1, 4 f_i)$) and the sensitivity experiment $\chi = 1 - \tanh(10 f_i)$ exhibit nearly identical seasonal cycles. This suggests that in these regions, the choice between attenuating mixing using a tangential hyperbolic shape or imposing a 25% of sea ice concentration limit for mixing yields similar outcomes. When the TKE penetration is turned off ($f_r = 0$), the seasonal cycle is very weak and the MLD is underestimated in winter. Increasing the fraction of surface TKE that penetrates into the ocean f_r from 0 to 0.1 increases the MLD as well as the amplitude of the seasonal cycle. As expected, a weaker-amplitude seasonal cycle is observed when varying the type of exponential decay h_τ from 30 to 10 m in high-latitude regions, as the TKE MLP vanishes more rapidly with depth.

During the summer months of July and August, all simulations underestimate the MLD compared to LOPS climatology. These summer biases could arguably be caused by the different reference depths used for computing the MLD with the density threshold criteria: 5 m for the LOPS climatology and 0.5 m for NEMO4.2. As shown by Treguier et al. (2023), the reference depth significantly impacts the MLD. For instance, changing the reference depth in the CMCC-NEMO model from 0.5 m to 10 m leads to differences in MLD exceeding 40 meters across large areas of the Southern Hemisphere oceans. In the Arctic region, these differences reach a few meters. However, we recomputed the MLD using the 5 m reference for the control run, and verified that such differences are not enough to explain the biases: the differences between the model MLDs computed with two reference depths were less than 5 m, and spatial patterns between the biases of observations and models were very similar (see Fig. A1 in the Appendix). To quantify the spatial variability of the mixed layer within each basin, we measure the MLD standard deviation for each month. The seasonal cycle of the MLD standard deviation during summer is almost negligible, and in winter, for the Makarov and Canada Basins, it remains below 15 m, showing a similar spatial variability between experiments in these regions (see Fig. A2 in Appendix). However, for the Eurasian Basin, differences between experiments appear to be more substantial. For instance, the MLD std reaches up to 30 m for the $\chi = 1$ experiment and is only 8 m for the $f_r = 0$ experiment.

A similar pattern emerges when examining the spatial distribution of the MLD. Fig 6 illustrates the differences between the sensitivity experiments and the control run for March and September. The largest ML deepening is observed for $\chi = 1$ (no attenuation of mixing due to sea ice coverage), with MDL at least 20 m thicker than the control run in both months across the studied regions. Similarly, $\chi = 1 - f_i$ leads to a comparable pattern, with deeper ML ranging from 10 to 20 m in both months. Conversely, the most significant ML shallowing is observed for $f_r = 0$ (TKE MLP turned off), resulting in ML shallower than the control by 20 m, particularly in the Canada and Eurasian Basins in March. Decreasing the characteristic depth of TKE penetration h_τ from 30 m to 10 m has an impact similar to a decrease of the penetrating fraction of energy f_r, with a similar spatial distribution in March and September. In the following, we will focus on three sensitivity experiments that differ the
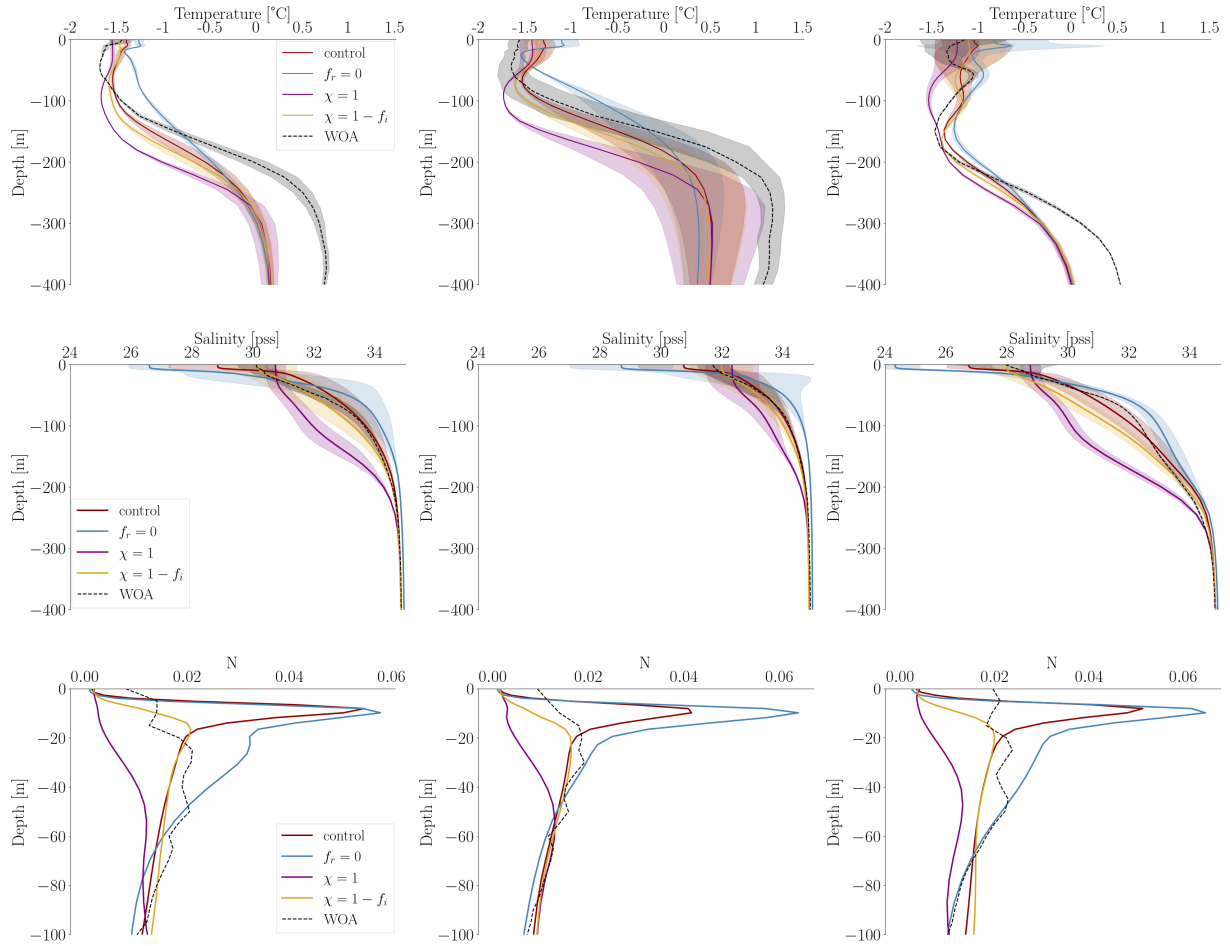
Figure 7. Vertical potential temperature in $^\circ C$, salinity in pss, and Brunt-Väisälä frequency (N) in the Makarov, Eurasian, and Canada Basins (from left to right) in September. The shaded areas represent the variance. Data is averaged over the period from 1970 to 2021. The dashed lines represent WOA climatology.

most from the control simulation: f_r (no TKE penetration) and $\chi = 1$ (full TKE MLP under sea ice), as well as $\chi = 1 - f_i$ (default sea-ice dependency of the parameterization, used in CMIP6).

Fig. 7 shows the vertical distribution of ocean physical properties in September, specifically the stratification, salinity, and temperature. To compare the stratification strength between the different simulations, we use the Brunt-Väisälä frequency, computed as

$$N = \sqrt{\frac{-g}{\rho}\frac{d\rho}{dz}} \tag{3}$$
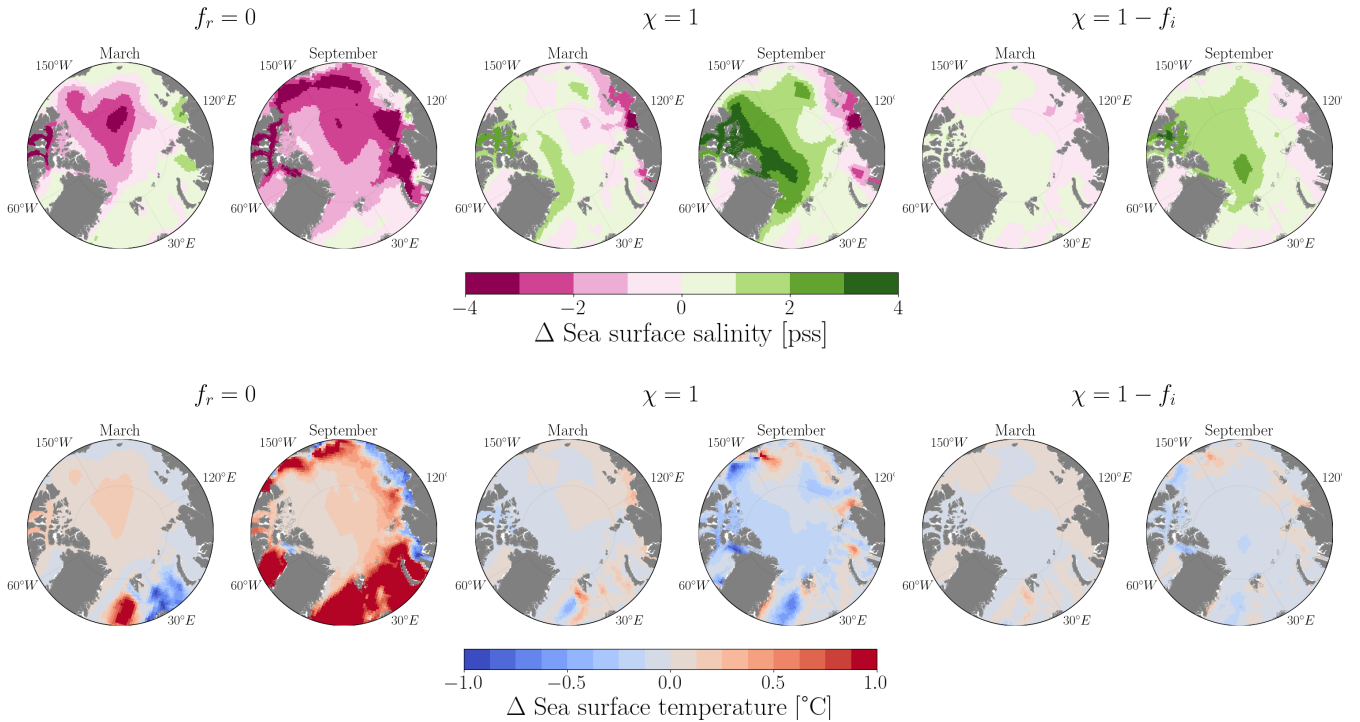
Figure 8. Sea surface salinity and potential temperature maps differences between sensitivity experiments and control simulation in March and September.

Where g represents the acceleration due to gravity approximated to $9.8\,m/s^2$, ρ is the potential density, and z is the vertical distance measured upward. Large values of N indicate a strong stratification and small values indicate a weak stratification. We
230   observe a strong stratification in the control run and the $f_r = 0$ experiment. On the contrary, the simulation with no attenuation of TKE MLP under sea ice is less stratified than the WOA climatology. This is in agreement with the MLD: with limited vertical mixing $f_r = 0$ a strong stratification is maintained in the upper layer, corresponding to shallow mixed layers. When TKE MLP is allowed under sea ice ($\chi = 1$), the upper ocean is less stratified and the MLD is larger. This suggests that the scaling parameter χ which governs the TKE MLP under sea ice significantly influences the stratification. In the control run
235   ($\chi = 1 - \min(1, 4f_i)$), TKE MLP vanishes as soon as the sea ice concentration reaches 25%, and there is not enough mixing (the stratification is too large compared to WOA climatology). This is improved when the TKE MLP varies proportionally to the sea ice concentration ($\chi = 1 - f_i$).

Regarding the vertical temperature profiles, we observe that compared to the control run, the $f_r = 0$ experiment shows an increase in upper ocean temperature, while the $\chi = 1$ and the $\chi = 1 - f_i$ experiments exhibit a slight decrease. The NEMO-SI3
240   simulations conducted here exhibit similar behavior to the OMIP1 and OMIP2 simulations analyzed by Allende et al. (2023). For example, referring to Fig. 6 in the mentioned paper, we can observe that the salinity and temperature profiles of the IPSL model resemble those of the $f_r = 0$ simulation (as expected, since they have deactivated the parameterization), while the CMCC

profiles resemble those of the $\chi = 1 - f_i$ simulation. As studied by Ilıcak et al. (2016), the NEMO models Kiel-ORCA05, NOC, CMCC, and CERFACS underestimate the maximum temperature because the Atlantic water is not well simulated in this model group (refer to Fig. 7 of Ilıcak et al. (2016)). While our control simulation demonstrates improvements compared to these models, adjusting the TKE MLP parameters does not improve the representation of the temperature maximum below 200 m, as this maximum is primarily affected by heat advection at that depth. The biases with the WOA climatology for the maximum temperature are approximately 0.5°C in all three basins. WOA climatology reaches values for maximum temperature of about 0.5, 1, and 0.5 °C in the Makarov, Eurasian, and Canada Basins, respectively. Similar maximum temperature values are observed using the PHC3.0 climatology in the Eurasian and Canada Basins, as noted by Ilıcak et al. (2016). Discrepancies between experiments are also observed in the vertical salinity profiles. Compared to the control run, the simulation with no TKE penetration ($f_r = 0$ experiment) exhibits the freshest conditions, with a decrease in salinity of at least 2 pss in the first tens of meters across all three basins. At the surface, salinity increases as TKE MLP intensifies; for example, in the $\chi = 1$ experiment, salinity increases by more than 2 pss compared to the control run across all three basins. The $\chi = 1 - f_i$ experiment yield upper ocean salinity values similar to those from the WOA climatology. In March, upper salinity differences between the experiments and the control run decrease for the $\chi = 1$ and the $\chi = 1 - f_i$ simulations in the three basins. However, they remain significant for the $f_r = 0$ simulation (see Fig. A3 in Appendix for March profiles). Compared to the WOA climatology, except for the no TKE penetration simulation, all the others exhibit higher upper ocean salinity in the Makarov and Eurasian Basins. In the Canada Basin, upper ocean salinity values are similar to those of the control run simulation.

The discrepancies between the sensitivity experiments and the control run for the spatial distribution of sea surface salinity and sea surface temperature exhibit a similar pattern (see Fig.8). A decrease in the MLD with a strong stratification corresponds to a reduction in sea surface salinity and an increase in surface temperature compared to the control simulation. In contrast, an increase in MLD with a weak stratification is associated with an increase in sea surface salinity and a decrease in surface temperature. This can be attributed to the fact that a shallower mixed layer and a strong stratification result in less mixing during ice melt, leading to a fresh anomaly at the surface and trapping heat at the surface. On the other hand, a deeper mixed layer and a weak stratification allow freshwater to mix more deeply, resulting in higher surface salinity and facilitating vertical heat exchange.

3.2 Sea ice properties

Considering the impact of the TKE MLP parameterization on the upper ocean, we expect an impact on sea ice properties. For instance, higher sea surface salinity lowers the freezing point of seawater, delaying the formation of sea ice. Conversely, lower sea surface salinity raises the freezing point, promoting sea ice formation. Additionally, colder sea surface temperatures encourage sea ice formation, while warmer sea surface temperatures contribute to sea ice melt. Fig. 9 illustrates the spatial distribution of sea ice concentration and thickness from the control run and observational data in March and September. In March, the central Arctic Ocean is almost completely covered by sea ice, with concentration reaching nearly 100%, and sea ice thickness peaks between 2.5 and 3m. By September, the effects of summer melt become evident, leading to a noticeable reduction in both sea ice concentration and thickness. When comparing spatial patterns with observational data (OSI-SAF for
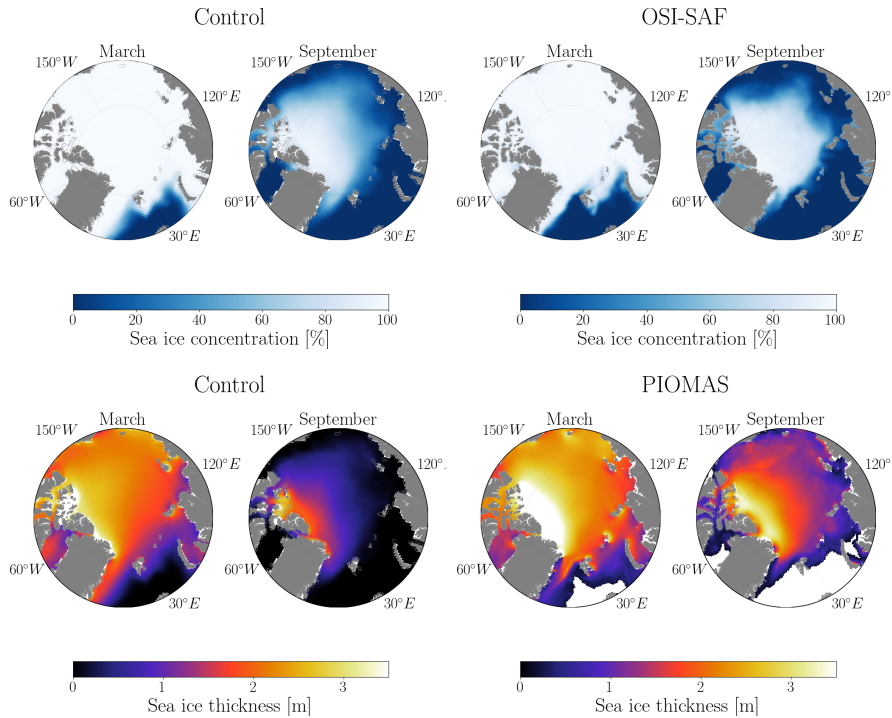
Figure 9. Maps of sea ice concentration and sea ice thickness for the control run and observational data in pan-Arctic regions during the months of March and September. The data has been averaged over the time period from 1970 to 2021 for the control run, and from 1979 to 2021 for observational data.

sea ice concentration and PIOMAS for sea ice thickness), NEMO-SI3 exhibits lower sea ice concentration and thickness in September. Specifically, regions near the East coast (Chukchi, East Siberian, Laptev, Kara, and Barents Seas) display sea ice thickness close to zero during this month. In March, negative biases between the simulated sea ice thickness and PIOMAS are more pronounced in the region next to Greenland. However, discrepancies between OSI-SAF and the simulated sea ice concentration seems to be relatively minor.

We analyze the seasonal cycle of sea ice concentration and thickness in the sensitivity experiments, control run, and observational data. Figure 10 illustrates these cycles across the Makarov, Eurasian, and Canada basins, with the model variables averaged from 1979 to 2021 to align with sea ice observational data. Compared with the OSI-SAF observational data, NEMO-SI3 performs well for sea ice concentration in winter months. However, during summer, the simulations underestimate sea ice concentration, with the most significant differences occurring in August, by approximately 30%, 48%, and 19% in Makarov, Eurasian, and Canada basins, respectively. These findings are consistent with similar observations made by Tsujino et al. (2020) for OMIP models, by Wang et al. (2016) for CORE models, and for coupled models studied in the CMIP5 and CMIP6 exercises by Shen et al. (2021) in the Arctic region. Regarding sea ice thickness, NEMO-SI3 generally simulates thinner sea ice thickness in comparison to the PIOMAS reanalysis. Compared to the control run, these biases amount to approximately
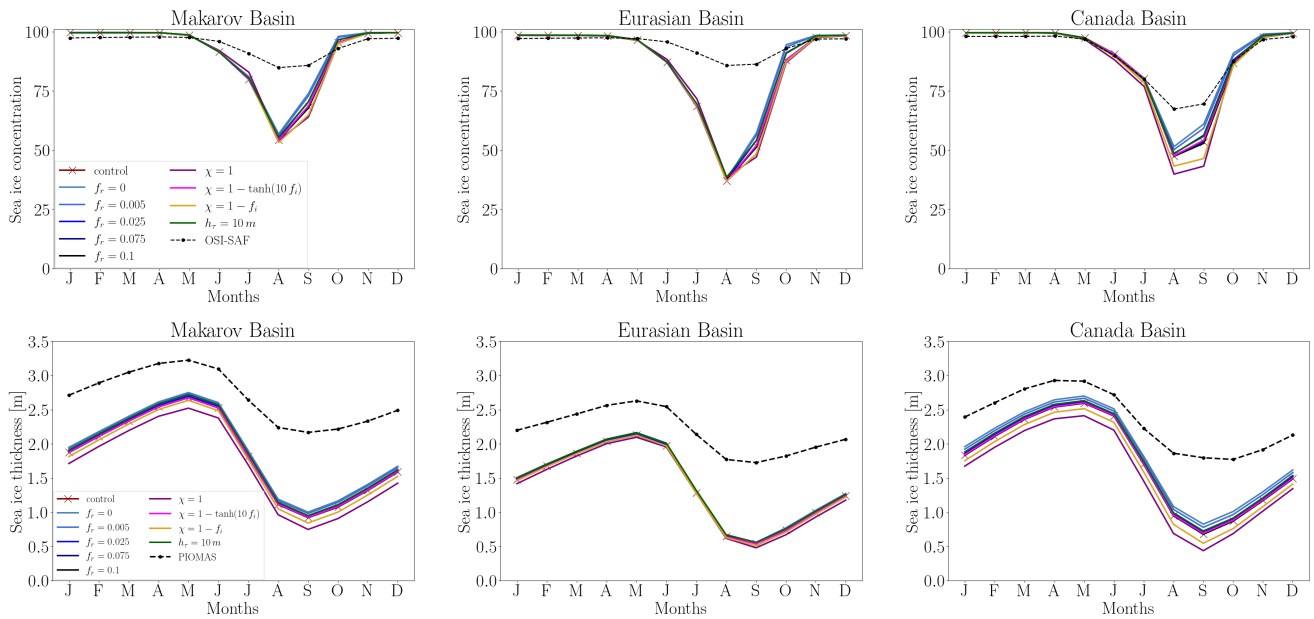
Figure 10. Seasonal cycle of the sea ice concentration and sea ice thickness in the Makarov, Eurasian and Canada Basins. Data is averaged in time between 1979–2021.

70, 57, and 44 cm in March in the Makarov, Eurasian, and Canada basins, respectively. In September, the discrepancies reach 1.1 m across the three basins. Similar results were observed by Rosenblum et al. (2021) in the Canada Basin.

Differences between the experiments are relatively small, except in the Canadian basin in summer. The simulation with no TKE MLP ($f_r = 0$) displays a 7% increase in sea ice concentration relative to the control case, while simulations with more
295   TKE MLP under sea ice ($\chi = 1$ and $\chi = 1 - f_i$) show a 10% and 7% decrease in September, respectively. A similar behavior is observed for sea ice thickness, with the largest differences between experiments observed in the Canada Basin. In September, in the $f_r = 0$ experiment, sea ice thickness increases by 14 cm; in the $\chi = 1$ experiment, sea ice thickness decreases by 24 cm; and the $\chi = 1 = f_i$ experiment shows a decrease of 13 cm in the sea ice thickness, relative to the control case. Fig. 11 shows the differences between the sensitivity experiments $f_r = 0$, $\chi = 1$ and $\chi = 1 = f_i$ with the control simulation. Notably, we observe
300   similar spatial patterns between sea ice thickness and sea ice concentration: an increase in sea ice for the $f_r = 0$ simulation and a decrease for the $\chi = 1$ and $\chi = 1 - f_i$ simulations. For the $\chi = 1$ simulation, a substantial reduction in sea ice—about more than 30 cm for sea ice thickness and 20 to 30% for sea ice concentration—is noticed in the area over the Beaufort gyre. While for the $\chi = 1 - f_i$ simulation, the spatial differences reach more than 10 cm. These discrepancies between experiments arise from variations in the density, salinity, and temperature vertical profiles (see Fig. 7). A strong stratification restricts vertical
305   mixing and its associated upward vertical heat flux. This reduction in vertical heat fluxes implies less exchange between the upper ocean and sea ice, resulting in reduced sea ice melt during the summer months, as observed in the experiment without
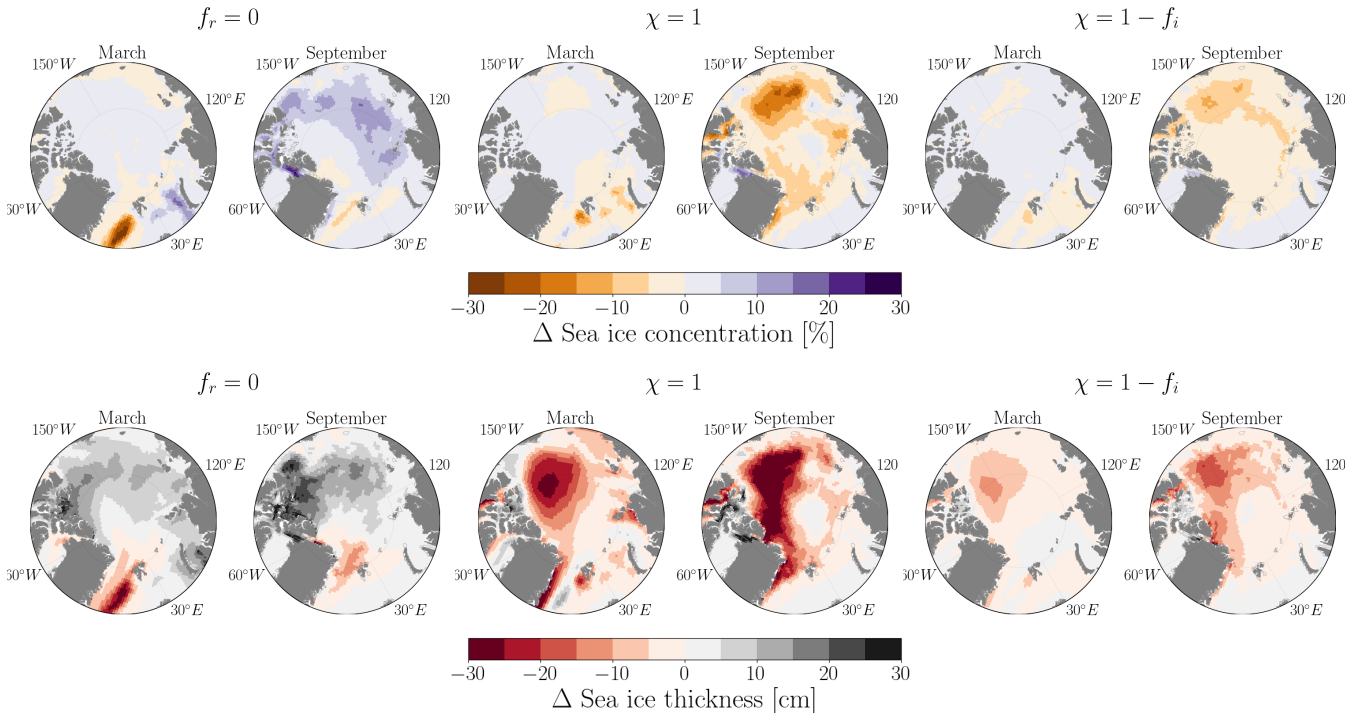
Figure 11. Maps of sea ice concentration and thickness differences between the sensitivity experiments and the control run in March and September. Data is averaged over the period from 1970 to 2021.

TKE MLP ($f_r = 0$). In contrast, a weak stratification enhances vertical mixing and heat flux, leading to increased sea ice melt, as seen in experiments with more TKE MLP under sea ice ($\chi = 1$ and $\chi = 1 - f_i$).

3.3 Inter-annual variability

We now examine the summer and winter inter-annual variability of the upper ocean and sea ice properties in the control run and three sensitivity experiments: $f_r = 0$, $\chi = 1$ and $\chi = 1 = f_i$. Fig. 12 displays the evolution of the MLD, sea ice concentration and sea ice thickness during the summer months of June to September. Previous studies by Cole and Stadler (2019) and Wei et al. (2024), utilizing ITP observational data, highlight the increase in the MLD in the Canada Basin since 2000. We also observe this trend in the MLD from ITP observational data in the three basins, where the linear regression slopes are 0.54, 0.37, and 0.19 m/year for the Makarov, Eurasian, and Canada Basins. It is important to note that while this trend is well-captured in the Canada Basin due to extensive ITP observations, the coverage in the Makarov and Eurasian Basins is limited (see Fig. A5 in Appendix). Although we observe an increase in the MLD in these regions, further data collection is necessary to fully assess the reliability of this trend.

Consistent with Fig. 5, all experiments simulate a ML shallower than observations, except for the $\chi = 1$ experiment with strong TKE MLP under sea ice, which exhibits a too depth seasonal cycle. Specifically, it underestimates the MLD in July
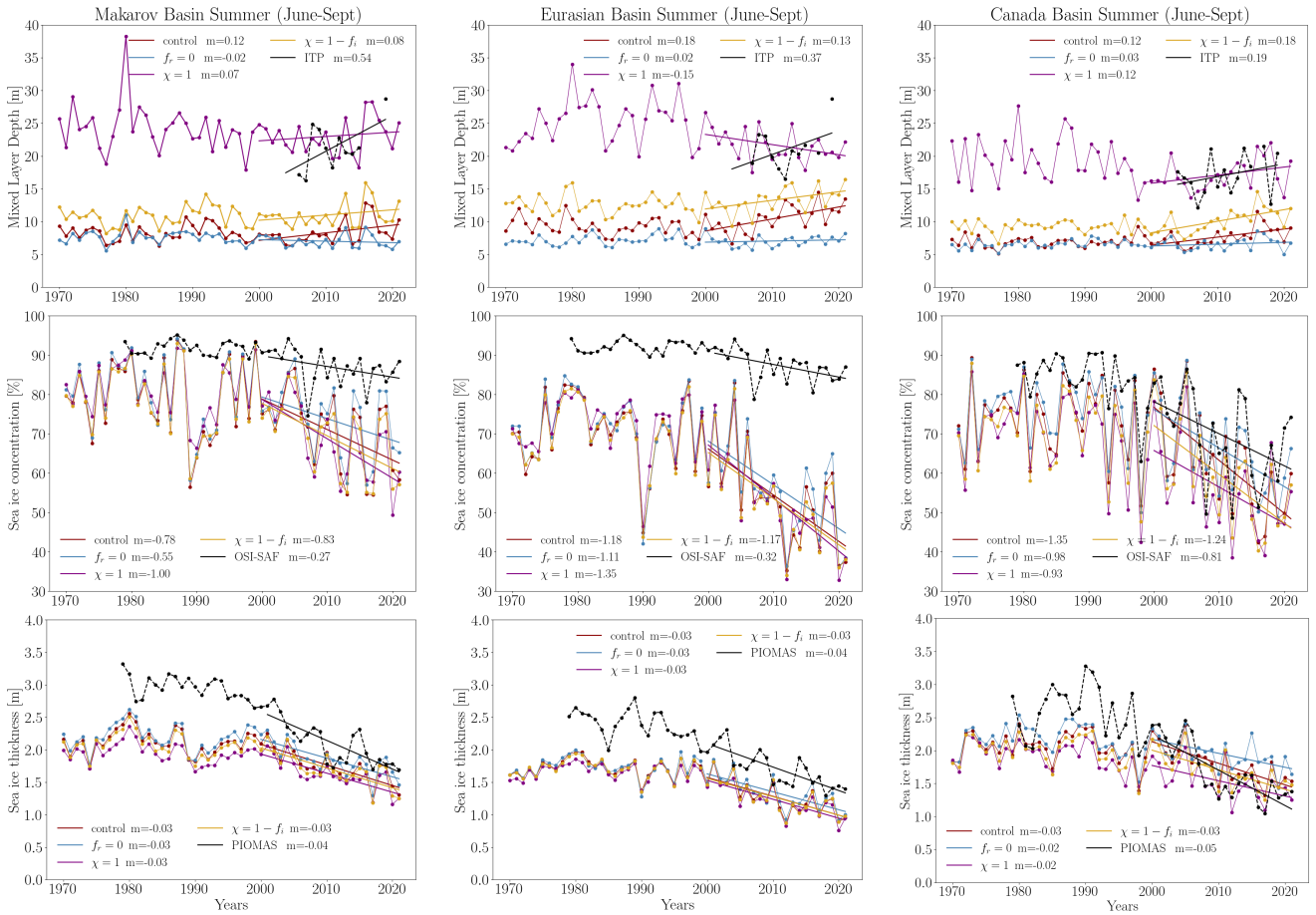
Figure 12. MLD, sea ice thickness and sea ice concentration for each summer (June to September) from 1970 to 2021 in the Makarov, Eurasian, and Canada Basins. Solid lines represent the linear regression, and m denotes the slope.

and August but overestimates it in June and September. We compute the same regression for sensitivity experiments within the same time frame (from 2000 to 2021). The $f_r = 0$ experiment (no TKE MLP) does not show an increase in the MLDAll other experiments display increasing trends in the three basins, except for the $\chi = 1$ experiment, which shows a slight decrease in the Eurasian Basin (m=-0.15 m/year).

325   We also compare the summer inter-annual variability of the simulated sea ice concentration and thickness with OSI-SAF observational data and PIOMAS reanalysis, respectively. Regarding sea ice concentration, significant biases are evident in the Eurasian Basin, whereas the simulated sea ice concentration aligns more closely with observational data in the Makarov and Canada basins. The experiments also underestimate the sea ice thickness compared to the PIOMAS data in the Makarov and Eurasian Basins, although the biases seem lower after year 2000. In the Canada Basin, the sea ice thickness is close to the PIOMAS reanalysis during the full period. Focusing on the trend from 2000 to 2021, both observational data and model simulations show a decrease in sea ice concentration in all three basins. The decrease is stronger in the model in the Makarov
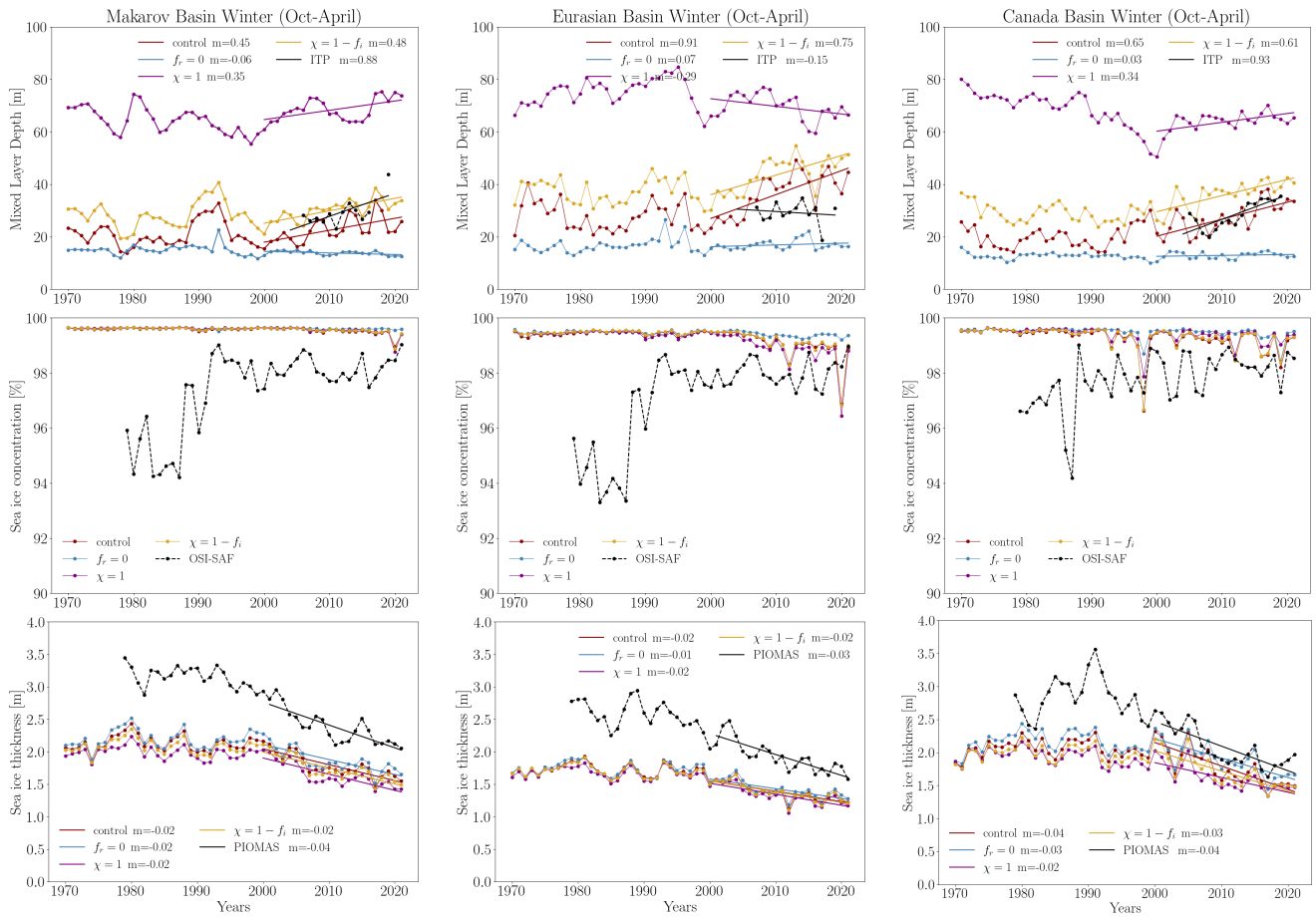
Figure 13. MLD, sea ice thickness and sea ice concentration for each winter (October to April) from 1970 to 2021 in the Makarov, Eurasian, and Canada Basins. Solid lines represent the linear regression, and m denotes the slope.

and Eurasian Basins compared with observations; for instance, the slopes of the linear regression reach -1.18 %/year for the control run and -0.32 %/year for the OSI-SAF data in the Eurasian Basin. However, in the Canada Basin, the NEMO-SI3 captures the decreasing trend in sea ice concentration quite well, with similar slopes for the sensitivity experiment linear regressions compared to the OSI-SAF one. This declining trend has been previously observed and studied by Tsujino et al. (2020), Stroeve and Notz (2018), and Cavalieri and Parkinson (2012) from both observational data and model simulations. This short-term trend (from 2000 to the present) is also evident in the simulated sea ice thickness and the sea ice thickness from the PIOMAS reanalysis in all three basins. The loss of sea ice thickness appears to be slower than that of sea ice concentration, with a slope of approximately -0.04 m/year for the PIOMAS reanalysis in all the basins.

Fig. 13 shows the winter inter-annual variability of the MLD, sea ice concentration, and sea ice thickness computed as the monthly average from October to April. As was the case in summer, the inter-model comparison reveals substantial differences in MLD. The overestimation of the MLD when TKE MLP is kept under sea ice ($\chi = 1$), also shown in Fig. 5, as well as

the underestimation when there is no TKE MLP ($f_r = 0$) are very clear. Comparing simulations with ITP observational data, the $\chi = 1 - f_i$ and control simulations exhibit closer resemblances. It has already been observed for the MLD seasonal cycle analysis. The increasing trend in MLD since 2000 is observed in ITP observational data in the Makarov and Canada Basins, with values for the linear regression slope being 0.88 and 0.93 m/year, respectively. Once again, the $\chi = 1 - f_i$ and control simulations closely resemble this behavior.

The winter inter-annual sea ice concentration reaches values close to 100%, dropping to around 98% in some years over the Canada Basin for all simulations except the one with vanished TKE MLP; those values are very similar to OSI-SAF observational data, except at the beginning of 1980 where the sea ice concentration decreases until 94%. Compared with PIOMAS reanalysis, larger sea ice thickness values are noted in the Makarov and Eurasian basins than those simulated. Simulated sea ice thickness ranges from 1.5 to 2 m, exhibiting a declining trend since 2000, consistent with trends observed in the PIOMAS reanalysis.

The decline of sea ice concentration since 2000 could explain the increase in the MLD for the $\chi = 1 - f_i$ and control run simulations ($\chi = 1 - \min(1, 4 f_i)$) because both parameterizations involve a scaling parameter depending on sea ice concentration. This is not the case for the other two cases, $\chi = 1$, where TKE MLD is present everywhere, and $f_r = 0$, where TKE MLP is not activated. Indeed, when we look at the summer and winter inter-annual variability in the Canada Basin for the full set of sensitivity experiments (see Fig. A4 in Appendix), we observe that the MLD increase is present for the large part of the experiments, except the full TKE MLP ($\chi = 1$) and those having a small percentage of the surface TKE penetrating in the ocean ($f_r = 0$ and $f_r = 0.005$).

4 Discussion and conclusion

We analyzed the NEMO-SI3 model's response to changes in the TKE MLP scheme within the central Arctic Ocean, focusing specifically on the Makarov, Eurasian, and Canada basins. This parameterization is governed by three key parameters: f_r, which denotes the fraction of surface TKE that penetrates into the ocean; h_τ, representing the vertical mixing length scale that controls the exponential shape of the penetration; and the scaling parameter χ in response to the presence of sea ice. As noted by Calvert and Siddorn (2013), Rodgers et al. (2014) and Storkey et al. (2018), the additional source of mixing by TKE MLP is beneficial in the NEMO model to reach realistic MLD in the Southern Ocean and in open water regions, which we demonstrate holds true for the Arctic region as well (see Table. 2). Our extreme experiment $\chi = 1$ shows that this source of mixing needs to be attenuated in the presence of sea ice. This is obvious from a physical point of view, because sea ice isolates the ocean from the atmosphere and damps inertial oscillations (Rainville et al., 2011). We have compared different functional forms for this attenuation. $\chi = 1 - f_i$ is the default option in NEMO, used in most CMIP6 projections, which displays a good agreement for the seasonal cycle of the MLD in the Makarov Basin. However, it results in a stronger seasonal cycle of the MLD compared with observations over the Eurasian and Canada Basins. The two other options $\chi = 1 - \tanh(10 f_i)$ and $\chi = 1 - \min(1, 4 f_i)$ behave similarly and produce a seasonal cycle of MLD closer to the LOPS climatology in these regions than the $1 - f_i$ option. Nevertheless, during summer all experiments underestimate the MLD over the three basins compared to the LOPS climatology.

Moreover, we noticed that the choice of the scaling parameter significantly affects ocean stratification and the density profile over the first 30 m of depth. We observed that changes in stratification are consistent with the changes in MLD: stronger stratification corresponds to shallower MLD, while weaker stratification corresponds to deeper MLD. These changes imply significant differences in salinity near the surface. We identified an increase in salinity for simulations with an increased MLD. Conversely, simulations with decreased MLD exhibited a decrease in sea surface salinity.

Regarding the inter-annual variability of the MLD, we detected a short-term trend of MLD from ITP observational data since 2000 in the three basins during summer and winter. It is important to highlight that while this trend is well-captured in the Canada Basin due to extensive ITP observations, their coverage in the Makarov and Eurasian Basins is limited. Although we observed an increase in the MLD in all three regions, further data collection is necessary to assess whether the ML is deepening not only in the Canada Basin but also in the Makarov and Eurasian Basins. The simulations with no TKE MLP do not represent the MLD trends. This raises questions regarding the choice made in some CMIP6 models to entirely remove TKE MLP, which may impact the representation of future arctic trends.

We have investigated for the first time whether the TKE MLP scheme influences sea ice concentration and thickness. For instance, we found a reduction of sea ice thickness from 30 to 40 cm compared to the control case when mixing was large under sea ice ($\chi = 1$) or not completely turned off ($\chi = 1 - f_i$). Conversely, the suppression of TKE MLP created a moderate increase in sea ice thickness, ranging from 10 to 20 cm. These discrepancies between experiments derive from variations in the density, salinity and temperature vertical profiles. Higher salinity in the upper layer lowers the seawater freezing point, thereby delaying sea ice formation. Conversely, lower sea surface salinity raises the freezing point, facilitating sea ice growth. Moreover, strong stratification restricts vertical mixing and its associated upward vertical heat flux, whereas weak stratification enhances both vertical mixing and heat flux.

This parameterization has been widely utilized in the NEMO community. Based on our study and considering the need to provide a comprehensive recommendation for NEMO users, we found that, in general, using sea ice attenuation $\chi = 1 - \min(1, 4f_i)$ (control run) or $\chi = 1 - \tanh(10f_i)$ produces more realistic results for the MLD and does not worsen the reproduction of sea ice. Therefore, we recommend continuing to use these parameterizations, which additionally use $f_r = 0.08$ and $h_\tau = 30$ m. However, it is important to note that the $\chi = 1 - f_i$ simulation seemed to have better agreement with sea surface salinity and temperature when compared to the LOPS climatology. Moreover, the vertical properties, especially ocean stratification, appeared to be highly dependent on this attenuation parameter. A deeper understanding of this parameter is needed to improve the TKE MLP parameterization. The underestimation of sea ice thickness and sea ice concentration in the control run remains in all sensitivity experiments, which show that these biases are not due to vertical mixing only. One potential reason for this could be the ERA5 forcing, which introduce warmer temperatures in the Arctic. As shown by Batrak and Müller (2019), ERA5 has a warm bias in winter, leading to thinner ice and a reduced summer extent in the model. Further investigation is needed to explore this aspect. Additionally, while this study has primarily focused on the Arctic region due to the availability of observational data for validation, it is important to evaluate how our various simulations perform in other sea-ice-covered regions.

The TKE MLP parameterization aims to reproduce the upper ocean vertical mixing driven by near-inertial oscillations, ocean swells, and waves. However, this parameterization lacks a physical basis and is considered "ad hoc" (Rodgers et al., 2014). More generally, the complexity of the various TKE options has led some groups to use the generalized length scale approach instead of the "historical" TKE vertical mixing scheme (Reffray et al., 2015). Another alternative vertical mixing scheme has been developed as part of the UK OSMOSIS project, planned to be included in the UK Global Ocean GO8 (Storkey et al., 2018). This initiative aims to refine near-surface oceanic mixing characterization through a combination of observational campaigns and a novel mixing scheme derived from extensive large eddy simulations. Future research should deepen our understanding of the underlying mechanisms driving the TKE MLP parameterization and explore alternative approaches to improve the robustness and accuracy of vertical mixing parameterizations in NEMO, especially in the presence of sea ice. Such efforts will be crucial for enhancing the fidelity of Arctic climate projections and advancing our understanding of polar climate dynamics.

Code and data availability. The NEMO version 4.2.1 utilized in this study is accessible in Zenodo via Allende (2024). For detailed information on version 4.2.1 utilized in this study, refer to the official user guide. For additional details regarding the latest version of the NEMO code, please refer to the NEMO's official repository. Model outputs, simulation details, and Python scripts to reproduce our figures are available in the supplementary materials provided by Allende Contador (2024).

Appendix A

A1

We here compile additional figures related to: MLD maps illustrating the differences between MLD from different reference depth criteria (Fig. A1); standard deviation seasonal cycle of the MLD in the Makarov, Eurasian and Canada Basin (Fig. A2); vertical temperature, salinity and Brunt-Väisälä frequency in the Makarov, Eurasian, and Canada Basins in March (Fig. A3); MLD inter-annual variability in summer and winter in the Canada Basin (Fig. A4); and MLD map from ITP data over the Arctic Ocean (Fig. A5).

Table 2. Performance Summary of TKE MLP experiments

Performance	Region	Seasonal Cycle MLD	Interannual Var MLD (Winter)	Seasonal Cycle Sea Ice Thick.	Interannual Var Sea Ice Thick. (Winter)
Good	Makarov Basin	$\chi = 1 - f_i$	control $f_r = 0.075, 0.1$ $\chi = 1 - f_i$ $\chi = 1 - \tanh(10 f_i)$	–	–
	Eurasian Basin	control $f_r = 0.075, 0.1$ $\chi = 1 - \tanh(10 f_i)$	control $f_r = 0.075, 0.1$ $\chi = 1 - \tanh(10 f_i)$	–	–
	Canada Basin	control $f_r = 0.075, 0.1$ $\chi = 1 - \tanh(10 f_i)$	control $f_r = 0.075, 0.1$ $\chi = 1 - \tanh(10 f_i)$	–	–
Intermediate	Makarov Basin	control $f_r = 0.075, 0.1$ $\chi = 1 - \tanh(10 f_i)$	–	–	–
	Eurasian Basin	$\chi = 1 - f_i$	$\chi = 1 - f_i$	–	–
	Canada Basin	$\chi = 1 - f_i$	$\chi = 1 - f_i$	control fr all $\chi = 1 - \tanh(10 f_i)$ $h_\tau = 10$ m	all
Bad	Makarov Basin	$\chi = 1$ $f_r = 0, 0.005, 0.025$ $h_\tau = 10$ m	$\chi = 1$ $f_r = 0, 0.005, 0.025$ $h_\tau = 10$ m	all	all
	Eurasian Basin	$\chi = 1$ $f_r = 0, 0.005, 0.025$ $h_\tau = 10$ m	$\chi = 1$ $f_r = 0, 0.005, 0.025$ $h_\tau = 10$ m	all	all
	Canada Basin	$\chi = 1$ $f_r = 0, 0.005, 0.025$ $h_\tau = 10$ m	$\chi = 1$ $f_r = 0, 0.005, 0.025$ $h_\tau = 10$ m	$\chi = 1$ $\chi = 1 - f_i$	–
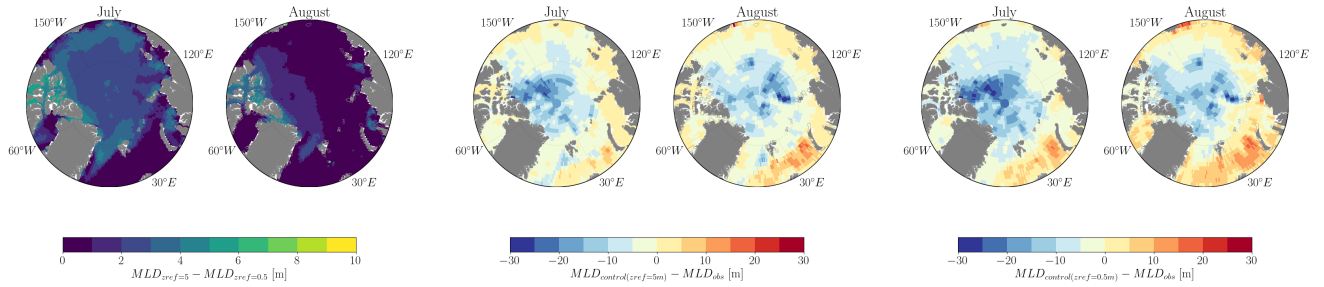
Figure A1. MLD maps illustrating the differences between the MLD from the control run computed at $z_{ref} = 5$m and $z_{ref} = 0.5$m, as well as the corresponding differences with the LOPS climatology during July and August.
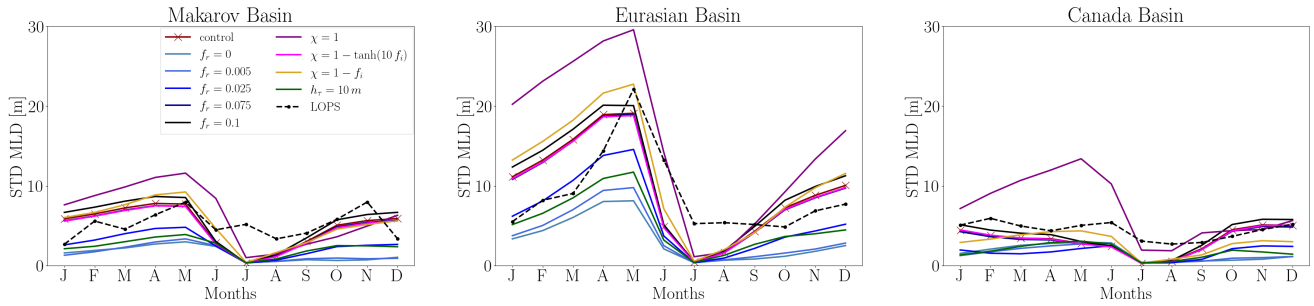
Figure A2. Standard deviation seasonal cycle of the MLD in the Makarov, Eurasian and Canada Basin. Data is averaged in time between 1970-2021.
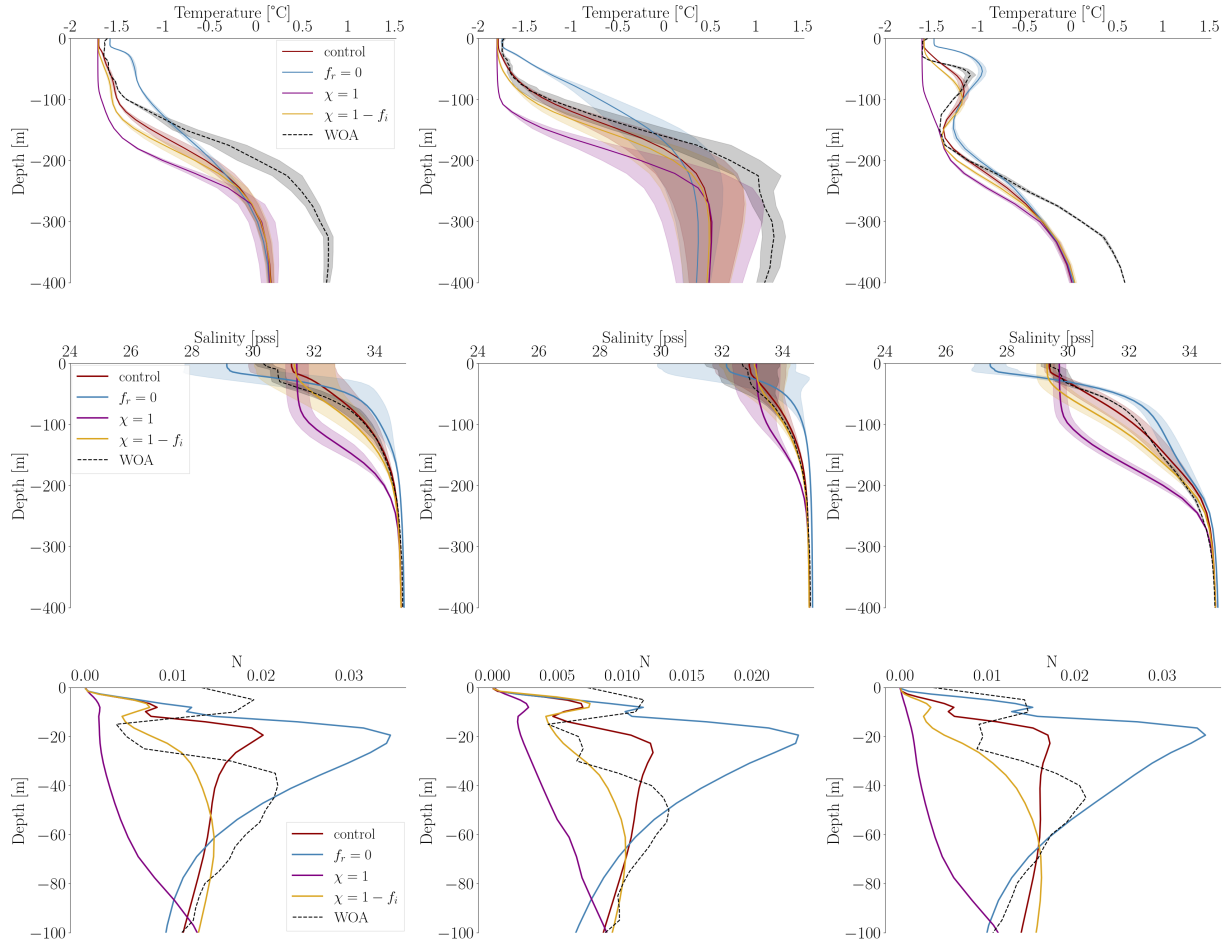
Figure A3. Vertical temperature in $^{\circ}C$, salinity in pss, and Brunt-Väisälä frequency (N) in the Makarov, Eurasian, and Canada Basins (from left to right) in March. The shaded areas represent the variance. Data is averaged over the period from 1970 to 2021. The dashed lines represent WOA climatology.
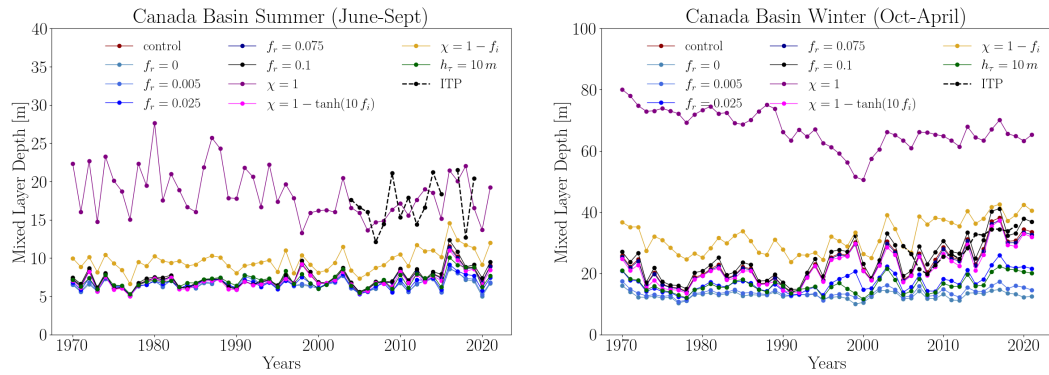
Figure A4. MLD inter-annual variability in summer (June to September) and winter (October to April) from 1970 to 2021 in the Canada Basin.
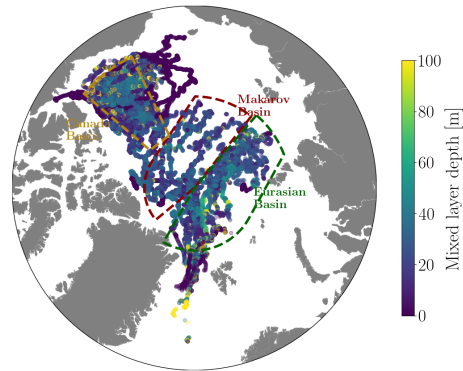
Figure A5. MLD map from ITP data over the Arctic Ocean. Dashed-lines represent the boundaries of the Makarov Basin, Eurasian Basin, and Canadian Basins.

Author contributions. SA, AMT, and CL collectively contributed to conceptualizing the research outlined in this paper. SA conducted the simulations, performed the statistical analyses, and created all the figures. SA took the lead in writing the manuscript, with contributions from AMT, CL, CDB, FM, TF, and AB.

435 *Competing interests.* The authors declare that they have no known competing financial interests or personal relationships that could have appeared to influence the work reported in this paper.

Acknowledgements. This work was conducted within the JPI Oceans and Climate project MEDLEY (MixED LayEr heterogeneitY), which is partly funded by the Belgian Science Policy Office under contract BE/20E/P1/MEDLEY; and by the French Agence Nationale pour la Recherche under contract 19-JPOC-0001-01.

440 Computational resources have been provided by the supercomputing facilities of the Université catholique de Louvain (CISM/UCL) and the Consortium des Équipements de Calcul Intensif en Fédération Wallonie Bruxelles (CÉCI) funded by the Fond de la Recherche Scientifique de Belgique (F.R.S.-FNRS) under convention 2.5020.11 and by the Walloon Region

References

Allende, S.: sofiallende/nemo: v4.2.1, https://doi.org/10.5281/zenodo.10732752, 2024.

445 Allende, S., Fichefet, T., Goosse, H., and Treguier, A.: On the ability of OMIP models to simulate the ocean mixed layer depth and its seasonal cycle in the Arctic Ocean, Ocean Modelling, 184, 102 226, 2023.

Allende Contador, S.: Sensitivity experiments of the parameters involved in the turbulent kinetic energy mixed layer penetration scheme of the NEMO ocean model, https://doi.org/10.14428/DVN/NZSKTU, 2024.

Axell, L.: Wind-driven internal waves and Langmuir circulations in a numerical ocean model of the southern Baltic Sea, Journal of Geophys-

450 ical Research: Oceans, 107, 25–1, 2002.

Batrak, Y. and Müller, M.: On the warm bias in atmospheric reanalyses induced by the missing snow over Arctic sea-ice, Nat. Commun., 10, 4170, 2019.

Blanke, B. and Delecluse, P.: Variability of the tropical Atlantic Ocean simulated by a general circulation model with two different mixed-layer physics, Journal of Physical Oceanography, 23, 1363–1388, 1993.

455 Bougeault, P. and Lacarrere, P.: Parameterization of orography-induced turbulence in a mesobeta–scale model, Monthly weather review, 117, 1872–1890, 1989.

Boyer, T., Baranova, O., Coleman, C., Garcia, H., Grodsky, A., Locarnini, R., Mishonov, A., Paver, C., Reagan, J., Seidov, D., et al.: Noaa atlas nesdis 87, World Ocean Database, pp. 1–207, 2018.

Brainerd, K. and Gregg, M.: Surface mixed and mixing layer depths, Deep Sea Research Part I: Oceanographic Research Papers, 42, 1521–

460 1543, 1995.

Calvert, D. and Siddorn, J.: Revised vertical mixing parameters for the UK community standard configuration of the global NEMO ocean model, Met Office Hadley Centre Technical Note, 95, 2013.

Cassotta, S., Derksen, C., Ekaykin, A., Hollowed, A., Kofinas, G., MAckintosh, A., Melbourne-Thomas, J., Muelbert, M., Ottersen, G., Pritchard, H., et al.: Special report on ocean and cryosphere in a changing chapter Intergovernmental Panel on Climate Change (IPCC),

465 in: Chapter 3 Polar Issues, Cambridge University Press, 2022.

Cavalieri, D. and Parkinson, C.: Arctic sea ice variability and trends, 1979–2010, The Cryosphere, 6, 881–889, 2012.

Cole, S. and Stadler, J.: Deepening of the winter mixed layer in the Canada basin, Arctic Ocean over 2006–2017, Journal of Geophysical Research: Oceans, 124, 4618–4630, 2019.

de Boyer Montégut, C., Madec, G., Fischer, A., Lazar, A., and Iudicone, D.: Mixed layer depth over the global ocean: An examination of

470 profile data and a profile-based climatology, Journal of Geophysical Research: Oceans, 109, https://doi.org/10.1029/2004JC002378, 2004.

de Boyer Montégut C.: Mixed layer depth over the global ocean: a climatology computed with a density threshold criterion of 0.03 kg/m3 from the value at the reference depth of 5 m, https://doi.org/10.17882/98226, 2024.

Docquier, D., Massonnet, F., Barthélemy, A., Tandon, N., Lecomte, O., and Fichefet, T.: Relationships between Arctic sea ice drift and strength modelled by NEMO-LIM3. 6, The Cryosphere, 11, 2829–2846, 2017.

475 Dong, C., Luo, X., Nie, H., Zhao, W., and Wei, H.: Effect of compressive strength on the performance of the NEMO-LIM model in Arctic Sea ice simulation, Journal of Oceanology and Limnology, 41, 1–16, 2023.

Ford, J., Pearce, T., Canosa, I., and Harper, S.: The rapidly changing Arctic and its societal implications, Wiley Interdisciplinary Reviews: Climate Change, 12, e735, 2021.

Gaspar, P., Grégoris, Y., and Lefevre, J.: A simple eddy kinetic energy model for simulations of the oceanic vertical mixing: Tests at station Papa and long-term upper ocean study site, Journal of Geophysical Research: Oceans, 95, 16 179–16 193, 1990.

Goosse, H., Allende Contador, S., Bitz, C., Blanchard-Wrigglesworth, E., Eayrs, C., Fichefet, T., Himmich, K., Huot, P., Klein, F., Marchi, S., et al.: Modulation of the seasonal cycle of the Antarctic sea ice extent by sea ice processes and feedbacks with the ocean and the atmosphere, The Cryosphere, 17, 407–425, 2023.

Hersbach, H., Bell, B., Berrisford, P., Hirahara, S., Horányi, A., Muñoz-Sabater, J., Nicolas, J., Peubey, C., Radu, R., Schepers, D., et al.: The ERA5 global reanalysis, Quarterly Journal of the Royal Meteorological Society, 146, 1999–2049, 2020.

Heuzé, C., Ridley, J., Calvert, D., Stevens, D., and Heywood, K.: Increasing vertical mixing to reduce Southern Ocean deep convection in NEMO3. 4, Geoscientific Model Development, 8, 3119–3130, 2015.

Ilıcak, M., Drange, H., Wang, Q., Gerdes, R., Aksenov, Y., Bailey, D., Bentsen, M., Biastoch, A., Bozec, A., Böning, C., et al.: An assessment of the Arctic Ocean in a suite of interannual CORE-II simulations. Part III: Hydrography and fluxes, Ocean Modelling, 100, 141–161, 2016.

Krishfield, R., Toole, J., and Timmermans, M.: ITP data processing procedures, Woods Hole Oceanographic Institution Tech. Rep, 24, 2008.

Lavergne, T., Sørensen, A., Kern, S., Tonboe, R., Notz, D., Aaboe, S., Bell, L., Dybkjær, G., Eastwood, S., Gabarro, C., et al.: Version 2 of the EUMETSAT OSI SAF and ESA CCI sea-ice concentration climate data records, The Cryosphere, 13, 49–78, 2019.

Lenn, Y., Fer, I., Timmermans, M., and MacKinnon, J.: Mixing in the Arctic Ocean, in: Ocean mixing, pp. 275–299, Elsevier, 2022.

Madec, G., Delecluse, P., Imbard, M., and Levy, C.: Ocean general circulation model reference manual, Note du Pôle de modélisation, 1997.

Madec, G., Bourdallé-Badie, R., Bouttier, P., Bricaud, C., Bruciaferri, D., Calvert, D., Chanut, J., Clementi, E., Coward, A., Delrosso, D., et al.: NEMO ocean engine, 2017.

McDougall, T. J. and Barker, P. M.: Getting started with TEOS-10 and the Gibbs Seawater (GSW) oceanographic toolbox, Scor/iapso WG, 127, 1–28, 2011.

McPhee, M.: Air-ice-ocean interaction: Turbulent ocean boundary layer exchange processes, Springer Science & Business Media, 2008.

Mellor, G. and Blumberg, A.: Wave breaking and ocean surface layer thermal response, Journal of physical oceanography, 34, 693–698, 2004.

Peralta-Ferriz, C. and Woodgate, R.: Seasonal and interannual variability of pan-Arctic surface mixed layer properties from 1979 to 2012 from hydrographic data, and the dominance of stratification for multiyear mixed layer depth shoaling, Progress in Oceanography, 134, 19–53, 2015.

Perovich, D. and Richter-Menge, J.: Loss of sea ice in the Arctic, Annual review of marine science, 1, 417–441, 2009.

Rabe, B., Heuzé, C., Regnery, J., Aksenov, Y., Allerholt, J., Athanase, M., Bai, Y., Basque, C., Bauch, D., Baumann, T., et al.: Overview of the MOSAiC expedition: Physical oceanography, Elem Sci Anth, 10, 00 062, 2022.

Rainville, L., Lee, C., and Woodgate, R.: Impact of wind-driven mixing in the Arctic Ocean, Oceanography, 24, 136–145, 2011.

Rathore, S., de Lavergne, C., Madec, G., Sallée, J.-B., Ethé, C., Nasser, A., and Vancoppenolle, M.: Effects of improved tidal mixing in NEMO one-degree global ocean model, In preparation for Journal of Advances in Modeling Earth Systems, 2024.

Reagan, J., Boyer, T., García, H., Locarnini, R., Baranova, OK. Bouchard, C., Cross, S., Mishonov, A., Paver, C., Seidov, D., Wang, Z., and Dukhovskoy, D.: World ocean database 2023, 2023.

Reffray, G., Bourdalle-Badie, R., and Calone, C.: Modelling turbulent vertical mixing sensitivity using a 1-D version of NEMO, Geoscientific Model Development, 8, 69–86, 2015.

Rodgers, K., Aumont, O., Mikaloff Fletcher, S., Plancherel, Y., Bopp, L., de Boyer Montégut, C., Iudicone, D., Keeling, R., Madec, G., and Wanninkhof, R.: Strong sensitivity of Southern Ocean carbon uptake and nutrient cycling to wind stirring, Biogeosciences, 11, 4077–4098, 2014.

Rosenblum, E., Fajber, R., Stroeve, J., Gille, S., Tremblay, L., and Carmack, E.: Surface salinity under transitioning ice cover in the Canada Basin: Climate model biases linked to vertical distribution of fresh water, Geophysical Research Letters, 48, e2021GL094 739, 2021.

Rudels, B. and Carmack, E.: Arctic ocean water mass structure and circulation, Oceanography, 35, 52–65, 2022.

Sea-Ice-Working-Group, N. et al.: Sea Ice modelling Integrated Initiative (SI3) The NEMO sea ice engine, Scientific Notes of Climate Modelling Center (31), 2020.

Shen, Z., Duan, A., Li, D., and Li, J.: Assessment and ranking of climate models in Arctic Sea ice cover simulation: From CMIP5 to CMIP6, Journal of Climate, 34, 3609–3627, 2021.

Storkey, D., Blaker, A., Mathiot, P., Megann, A., Aksenov, Y., Blockley, E., Calvert, D., Graham, T., Hewitt, H., Hyder, P., et al.: UK Global Ocean GO6 and GO7: A traceable hierarchy of model resolutions, Geoscientific Model Development, 11, 3187–3213, 2018.

Stroeve, J. and Notz, D.: Changing state of Arctic sea ice across all seasons, Environmental Research Letters, 13, 103 001, 2018.

Toole, J., Krishfield, R., Timmermans, M., and Proshutinsky, A.: The ice-tethered profiler: Argo of the Arctic, Oceanography, 24, 126–135, 2011.

Treguier, A., de Boyer Montégut, C., Bozec, A., Chassignet, E., Fox-Kemper, B., Hogg, A., Iovino, D., Kiss, A., Le Sommer, J., Li, Y., et al.: The mixed layer depth in the ocean model intercomparison project (OMIP): Impact of resolving mesoscale eddies, EGUsphere, 2023.

Tsujino, H., Urakawa, L., Griffies, S. M., Danabasoglu, G., Adcroft, A., Amaral, A., Arsouze, T., Bentsen, M., Bernardello, R., Böning, C., et al.: Evaluation of global ocean–sea-ice model simulations based on the experimental protocols of the Ocean Model Intercomparison Project phase 2 (OMIP-2), Geoscientific Model Development, 13, 3643–3708, 2020.

Vancoppenolle, M., Fichefet, T., Goosse, H., Bouillon, S., Beatty, C., and Maqueda, M. M.: LIM3, an advanced sea-ice model for climate simulation and operational oceanography, Mercator Newsletter, 28, 16–21, 2008.

Wang, Q., Ilicak, M., Gerdes, R., Drange, H., Aksenov, Y., Bailey, D., Bentsen, M., Biastoch, A., Bozec, A., Böning, C., et al.: An assessment of the Arctic Ocean in a suite of interannual CORE-II simulations. Part I: Sea ice and solid freshwater, Ocean Modelling, 99, 110–132, 2016.

Wei, G., Liu, H., and Cai, L.: The Oceanic Mixed Layer Changes Along with the State Transition of the Beaufort Gyre, Dynamics of Atmospheres and Oceans, p. 101446, 2024.

Zhang, J. and Rothrock, D.: Modeling global sea ice with a thickness and enthalpy distribution model in generalized curvilinear coordinates, Monthly Weather Review, 131, 845–861, 2003.